

1. Introduction

New antireflection coatings offer advantages of both broadband antireflection and wide angle antireflection. Recently, we utilized Bayesian learning optimization with finite difference time domain simulations to determine the optimized antireflection properties of single layer thin film, nanowire arrays, and nanocone arrays, which are shown in Fig. 1 [1]. Sub-wavelength nanostructures have been of interest for their broadband and broad angle antireflection properties [2, 3]. Our simulations demonstrated that nanowire arrays and single layer thin films have comparable antireflection performance. The best nanowire array has an effective index of refraction similar to that of an optimized thin film with an index of refraction that is the geometric mean of the glass and air. In contrast, the nanocone arrays demonstrate superior antireflection performance where they are able to grade the index of refraction between the air and the glass. Nanocone arrays are able to achieve solar integrated normal reflection of 0.15% and solar integrated 65 °incidence of 1.25%. Such structures could be created in glass via maskless reactive ion etching methods [4, 5] or other patterning methods [6].

Both broadband and broad angle antireflection may have benefits for solar modules, which are typically fixed installations as opposed to tracking due to the economic costs associated with tracking [7]. Fixed installations are often installed at non-ideal orientations and tilts as, for example, the existing orientation and slope of a roof may be used. In addition, diffuse radiation from the sky and ground reflected radiation also result in light hitting the solar module across a variety of non-normal incidence angles. It is not clear what power generation enhancements can be expected due to these antireflection structures under different fixed and tracking configurations.

Fig. 1 shows the optimized structures previously determined from Bayesian optimization [1]. The single layer thin film consists of a single dielectric with an index of refraction of the geometric mean of glass and air or $n_1 = 1.21$ and thickness $t = 120$ nm. The nanowire array has a pitch $a = 390$ nm, a diameter of $d = 290$ nm, and a height of $h = 150$ nm. The nanocone has a pitch $a = 400$ nm, bottom diameter $d_{bot} = 400$ nm, top diameter $d_{top} = 90$ nm, and height $h = 640$ nm.

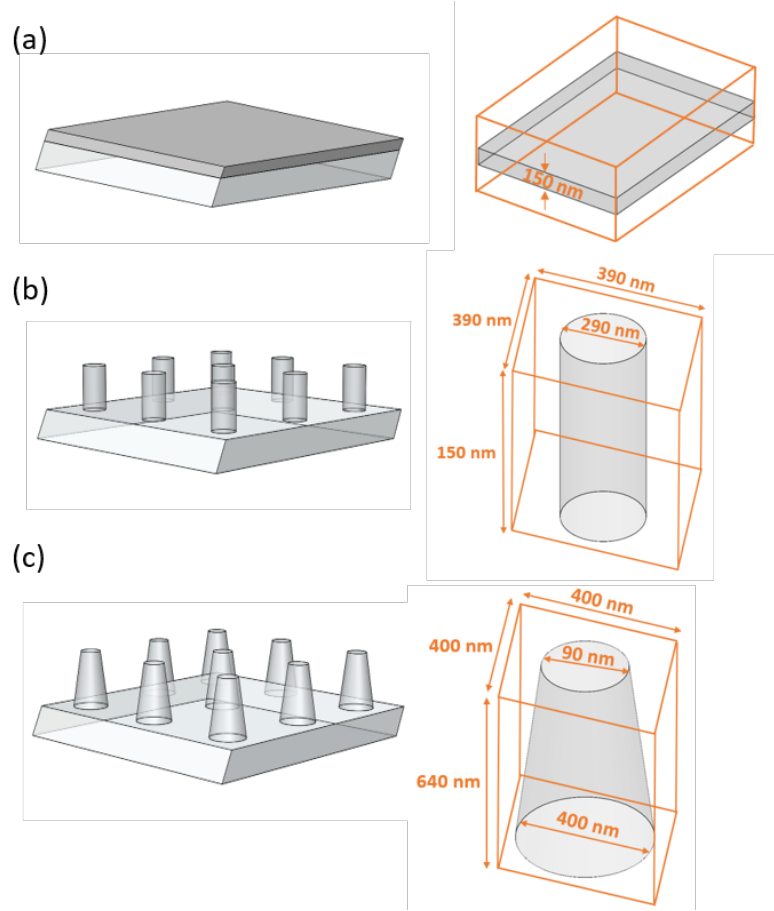


Figure 1: Structures and dimensions of the (a) thin film, (b) nanowire, and (c) nanocone simulated in this study.

Use true dimensions in schematic

Maybe different color than orange.

The full reflection spectra of these three structures were simulated by the finite difference time domain method (FDTD). The broadband fixed angle source technique is used to simulate the periodic structures with a broadband plane wave source illuminated at an angle [8]. The reflection spectra of various antireflection structures is shown in Fig. 2. The reflection is shown as a function of wavelength along the radius and incidence angle θ in the circumferential direction. The reflection is shown for (a)(i) bare glass, (ii) thin film, (iii) nanowire array, and (iv) nanocone array. The reflection spectra shown is averaged for both TE and TM polarized light and averaged

over the incident azimuth angles γ_i . The integrated reflection as a function of incidence angle θ is shown in Fig. 2(b). The reflection spectra is integrated over the AM1.5D solar spectrum [10] for wavelengths from 280 to 1200 nm. The bare glass has a solar integrated reflection of 3.73% at normal incidence compared to 0.80, 0.64, and 0.19% for the thin film, nanowire array, and nanocone array, respectively. The thin film and nanowire array have very similar antireflection performance over all the incidence angles, while the nanocone array also has the best antireflection properties across all incidence angles. At 60° incidence angle, the solar integrated reflection is 17.77, 4.11, 4.14, and 0.64%, for the bare glass, thin film, nanowire array, and nanocone array, respectively.

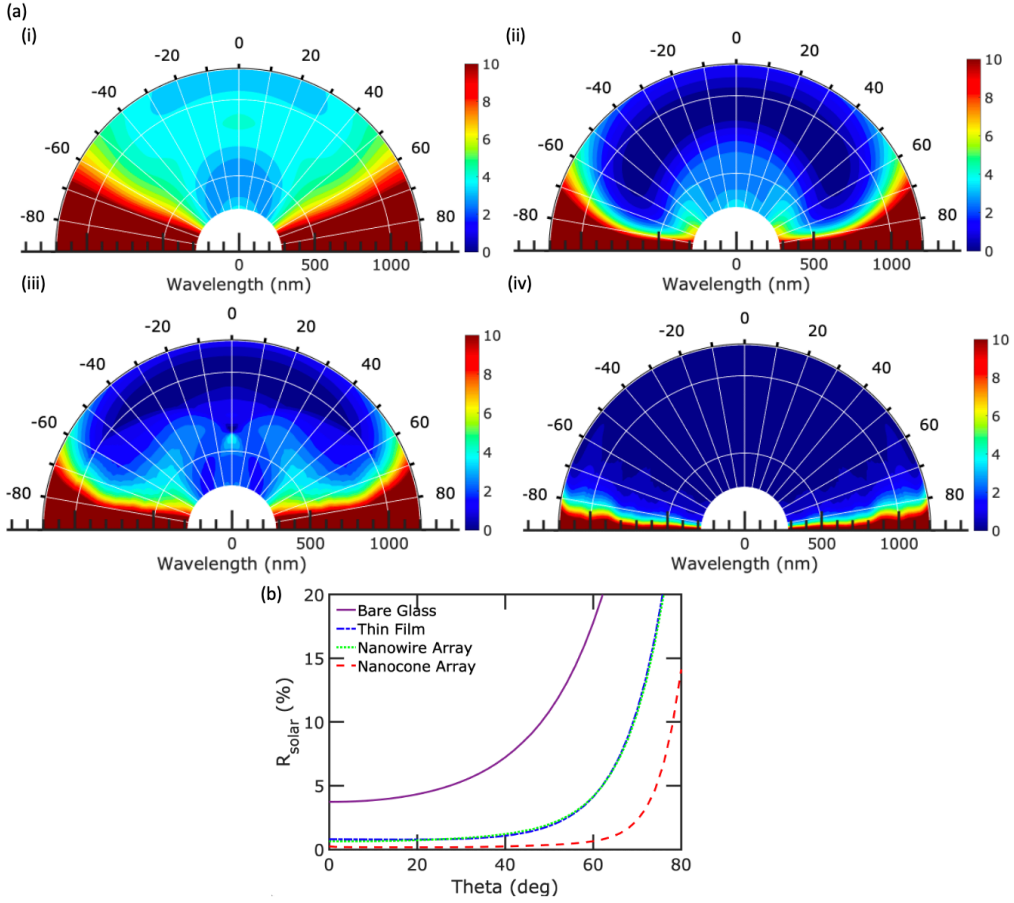


Figure 2: Reflection spectra of different structures. (a) Reflection spectra as a function of incidence angle θ for (i) bare glass, (ii) thin film, (iii) nanowire array, and (iv) nanocone array. (b) Integrated solar reflection as a function of incidence angle.

We combine this with a simple model for studying available solar irradiance for different module orientations and latitudes [9] to determine the annual enhancement of available solar irradiance with different types of antireflection coatings. The direct beam spectral irradiance $F(\lambda)$ of arbitrary airmass AM is

$$F_{bn}(\lambda, AM) = F_{AM0}(\lambda) \left[\frac{F_{AM1.5D}(\lambda)}{F_{AM0}(\lambda)} \right]^{(AM/1.5)^{0.678}} \quad (1)$$

where $F_{AM0}(\lambda)$ and $F_{AM1.5D}(\lambda)$ are the spectral irradiance of the AM0 and AM1.5D spectrum [10], respectively and λ is the wavelength in vacuum. The

power relationship is a fit to empirical data [11]. The air mass is defined by

$$AM = \frac{1}{\cos \theta_z} \quad (2)$$

where θ_z is the solar zenith angle. The direct beam irradiance of particular air mass may be obtained by integrating the direct beam spectral irradiance

$$I_{bn}(AM) = \int F_{bn}(\lambda) d\lambda. \quad (3)$$

The AM1.5G spectrum is assumed to follow the same scaling as AM1.5D and the diffuse radiation can be obtained from the difference between the global spectral irradiance and the direct beam spectral irradiance:

$$F_d(\lambda, AM) = F_{AM0}(\lambda) \left[\frac{F_{AM1.5G}(\lambda)}{F_{AM0}(\lambda)} \right]^{(AM/1.5)^{0.678}} - F_{bn} \quad (4)$$

where the diffuse irradiance is

$$I_d(AM) = \int F_d(\lambda) d\lambda. \quad (5)$$

The direct beam and diffuse photon flux density are related to the direct beam and diffuse spectral irradiance, respectively, by

$$b_{bn}(\lambda, AM) = \frac{F_{bn}(\lambda, AM)\lambda}{hc} \quad (6)$$

and

$$b_d(\lambda, AM) = \frac{F_d(\lambda, AM)\lambda}{hc}. \quad (7)$$

The total photon flux density incident on a module is the sum of the direct beam and diffuse components

$$b_{Tm}(\lambda, AM) = b_{bn}(\lambda, AM) \cos \theta + b_d(\lambda, AM) \frac{(1 + \cos \beta)}{2}. \quad (8)$$

where θ is the angle between the direct beam radiation on the module and the normal to the module surface. θ is limited to between 0° and 90° . β is the solar module tilt. $\beta = 0^\circ$ indicates the module is mounted horizontal and a positive slope indicates the module is tilted toward south in the northern hemisphere and toward north in the southern hemisphere.

The total photon flux incident on a module is

$$\Phi_m(AM) = \int b_{Tm}(\lambda) d\lambda \quad (9)$$

The annual module incident photon flux is

$$B_{mA} = \frac{12}{\pi} \times 3600 \int_0^{365} \int_{-\omega_s}^{\omega_s} \Phi_m(AM) d\omega dn \quad (10)$$

where ω_s is the sunset hour angle defined by

$$\omega_s = \cos^{-1}(-\tan \phi \tan \delta) \quad (11)$$

and $-\omega_s$ is the sunrise hour angle.

The number of incident photons reflected at the glass/air interface is

$$b_R = b_{bn}(\lambda, AM) R(\lambda, \theta, \gamma_i) \cos \theta + b_d(\lambda, AM) \frac{1}{2\pi} \int_0^{2\pi} \int_0^{\pi/2-\beta} \left(\frac{1 + \cos \theta}{2} \right) R(\lambda, \theta, \gamma_i) d\theta \quad (12)$$

where $R(\lambda, \theta, \gamma_i)$ is the reflection spectra of the module/interface is a function of angle of incidence θ , and injection azimuth angle γ_i . $\gamma_i = \gamma - \gamma_s$, where γ is the module azimuth angle and γ_s is the solar azimuth angle. The azimuth angle is defined so 0° is south, negative is east, and positive is west [12].

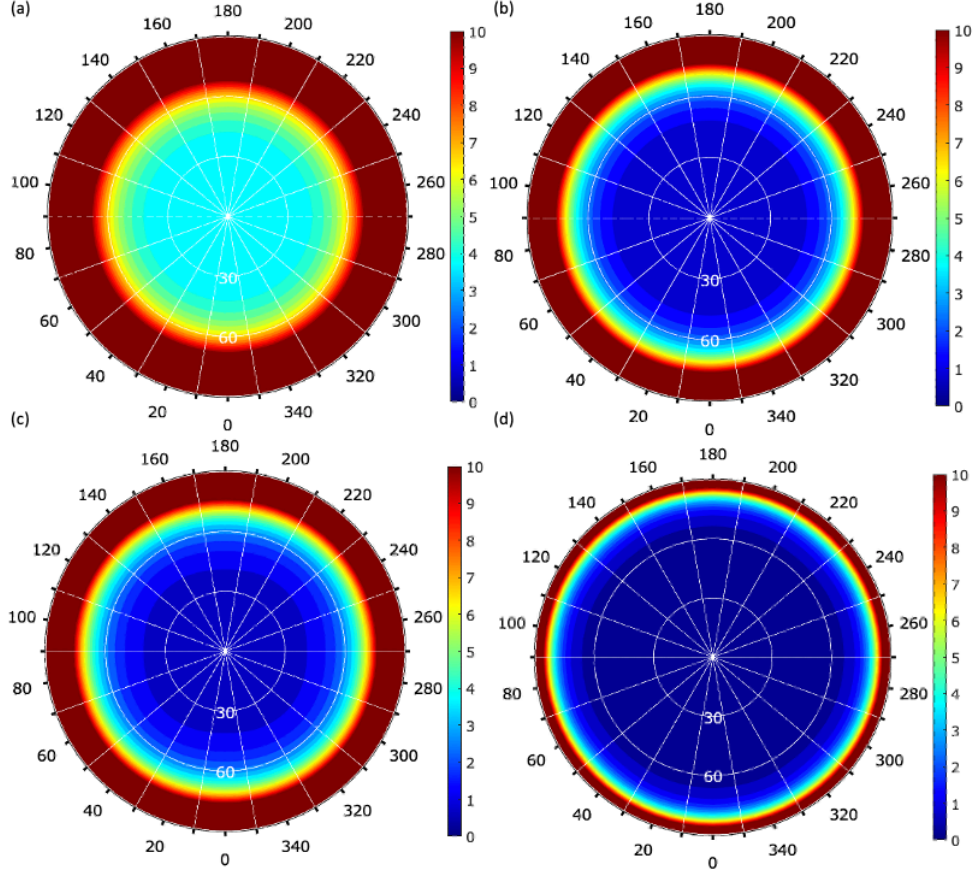


Figure 3: Polar plots of integrated solar reflection for (a) bare glass, (b) thin film, (c) nanowire array and (d) nanocone array. The incidence angle θ in degrees is shown along the radial direction and the azimuth angle γ_i in degrees along the circumference.

Fig. 3 plots the solar integrated reflection for the four structures as a function of incidence angle θ and azimuthal injection angle γ_i . The bare glass and thin film antireflection layer have no azimuthal angle injection angle dependence, whereas the the NW array and NC arrays both have very weak azimuthal angle injection angle dependence, and thus for simplifying the calculations we simply use the averaged azimuthal angle reflection of the different surfaces

$$b_R \approx b_{bn}(\lambda, AM) \tilde{R}(\lambda, \theta) \cos \theta + b_d(\lambda, AM) \int_0^{\pi/2-\beta} \left(\frac{1 + \cos \theta}{2} \right) \tilde{R}(\lambda, \theta) d\theta \quad (13)$$

where $\tilde{R}(\lambda, \theta)$ is the averaged reflection over all the azimuth directions.

The total photon flux reflected is

$$\Phi_R = \int b_R(\lambda) d\lambda \quad (14)$$

$$\Phi_R(\theta) = \cos \theta \int b_{bn}(\lambda) R(\lambda, \theta) d\lambda + \int_0^{\pi/2-\beta} \left(\frac{1 + \cos \theta}{2} \right) \int b_d(\lambda) R(\lambda, \theta) d\lambda d\theta \quad (15)$$

where the direct beam photon flux is

$$\Phi_{bn} = \int b_b(\lambda) d\lambda \quad (16)$$

and

$$R_s(\theta) = \frac{\int b_b(\lambda) R(\lambda, \theta) d\lambda}{\int b_b(\lambda) d\lambda} \quad (17)$$

The annual solar cell flux reflected is

$$B_{RA} = \frac{12}{\pi} \times 3600 \int_0^{365} \int_{-\omega_s}^{\omega_s} \Phi_R(\theta) d\omega dn \quad (18)$$

The annual module reflection is the portion of photons over an entire year that are lost due to reflection is

$$R_A = \frac{B_{RA}}{B_{mA}} \quad (19)$$

$$(20)$$

2. Data Availability

All python code used for the model to generate the figures in the manuscript can be found in the following Github repository:

<https://github.com/pleu/LAMPsolar>.

3. Acknowledgements

This work was supported by the National Science Foundation [grant number 1930582].

References

- [1] S. Haghanifar, M. McCourt, B. Cheng, J. Wuenschell, P. Ohodnicki, P. W. Leu, Discovering high-performance broadband and broad angle antireflection surfaces by machine learning, *Optica* 7 (7) (2020) 784–789. doi:10.1364/OPTICA.387938.
URL <http://www.osapublishing.org/optica/abstract.cfm?URI=optica-7-7-784>
- [2] G. S. Han, S. Lee, M. L. Duff, F. Qin, M. Jiang, G. Li, J.-K. Lee, Multi-functional transparent electrode for reliable flexible perovskite solar cells, *Journal of Power Sources* 435 (2019) 226768. doi:10.1016/j.jpowsour.2019.226768.
URL <https://www.sciencedirect.com/science/article/pii/S0378775319307396>
- [3] S. Haghanifar, A. J. Galante, P. W. Leu, Challenges and Prospects of Bio-Inspired and Multifunctional Transparent Substrates and Barrier Layers for Optoelectronics, *ACS Nano* 14 (12) (2020) 16241–16265, publisher: American Chemical Society. doi:10.1021/acsnano.0c06452.
URL <https://doi.org/10.1021/acsnano.0c06452>
- [4] S. Haghanifar, M. McCourt, B. Cheng, J. Wuenschell, P. Ohodnicki, a. P. W. Leu, Creating glasswing butterfly-inspired durable antifogging superomniphobic supertransmissive, superclear nanostructured glass through Bayesian learning and optimization,, *Materials Horizons*doi: doi:10.1039/C9MH00589G.
- [5] S. Haghanifar, T. Gao, R. T. R. D. Vecchis, B. Pafchek, T. D. B. Jacobs, P. W. Leu, Ultrahigh-transparency, ultrahigh-haze nanograss glass with fluid-induced switchable haze, *Optica* 4 (12) (2017) 1522–1525. doi:10.1364/OPTICA.4.001522.
URL <https://www.osapublishing.org/optica/abstract.cfm?URI=Optica-4-12-1522>
- [6] D. Infante, K. W. Koch, P. Mazumder, L. Tian, A. Carrilero, D. Tulli, D. Baker, V. Pruneri, Durable, superhydrophobic, antireflection, and low haze glass surfaces using scalable metal dewetting nanostructuring, *Nano Research* 6 (6) (2013) 429–440. doi:10.1007/s12274-013-0320-z.

URL <https://link.springer.com/article/10.1007/s12274-013-0320-z>

- [7] M. Bolinger, J. Seel, D. Robson, C. Warner, Utility-Scale Solar Data Update: 2020 Edition, Tech. rep., Lawrence Berkeley National Lab. (LBNL), Berkeley, CA (United States) (Nov. 2020). doi:10.2172/1706670.
URL <https://www.osti.gov/biblio/1706670>
- [8] B. Liang, M. Bai, H. Ma, N. Ou, J. Miao, Wideband Analysis of Periodic Structures at Oblique Incidence by Material Independent FDTD Algorithm, IEEE Transactions on Antennas and Propagation 62 (1) (2014) 354–360, conference Name: IEEE Transactions on Antennas and Propagation. doi:10.1109/TAP.2013.2287896.
- [9] S. P. Sharma, P. W. Leu, Solar module orientation and tracking type performance and optimization, Journal of Photonics for Energy 11 (4) (2021) 045501, publisher: SPIE. doi:10.1117/1.JPE.11.045501.
URL <https://www.spiedigitallibrary.org/journals/journal-of-photonics-for-energy/volume-11/issue-4/045501/Solar-module-orientation-and-tracking-type-performance-and-optimization/10.1117/1.JPE.11.045501.full>
- [10] Reference Air Mass 1.5 Spectra (2020).
URL <https://www.nrel.gov/grid/solar-resource/spectra-am1.5.html>
- [11] A. B. Meinel, Applied Solar Energy: An Introduction, Addison-Wesley, Reading, 1976.
- [12] J. A. Duffie, W. A. Beckman, Solar Engineering of Thermal Processes, John Wiley & Sons, Incorporated, Somerset, UNITED STATES, 2013.
URL <http://ebookcentral.proquest.com/lib/pitt-ebooks/detail.action?docID=1162079>